Article

Bimolecular versus Trimolecular Reaction Pathways for H_2O_2 with Hypochlorous Species and Implications for Wastewater Reclamation

Zonghao Luo, Wenjing Zhou, Ying Jiang, Daisuke Minakata, Richard Spinney, Dionysios D. Dionysiou, Jianbo Liu,* and Ruiyang Xiao*

Read Online

ACCESS | Metrics & More | Article Recommendations | Supporting Information

ABSTRACT: The benchmark advanced oxidation technology (AOT) that uses UV/H_2O_2 integrated with hypochlorous species exhibits great potential in removing micropollutants and enhancing wastewater treatability for reclamation purposes. Although efforts have been made to study the reactions of H_2O_2 with hypochlorous species, there exist great discrepancies in the order of reaction kinetics, the rate constants, and the molecule-level mechanisms. This results in an excessive use of hypochlorous reagents and system underperformance during treatment processes. Herein, the titled reaction was investigated systematically through complementary experimental and theoretical approaches. Stopped-flow spectroscopic measurements revealed a combination of bi- and trimolecular reaction kinetics. The bimolecular pathway dominates at low H_2O_2 concentrations, while the trimolecular pathway dominates at high H_2O_2 concentrations. Both reactions were simulated using direct dynamics trajectories, and the pathways identified in the trajectories were further validated by high-level quantum chemistry calculations. The theoretical results not only supported the spectroscopic data but also elucidated the molecule-level mechanisms and helped to address the origin of the discrepancies. In addition, the impact of the environmental matrix was evaluated by using two waters with discrete characteristics, namely municipal wastewater and ammonium-rich wastewater. Municipal wastewater had a negligible matrix effect on the reaction kinetics of H_2O_2 and the hypochlorous species, making it a highly suitable candidate for this integration technique. The obtained in-depth reaction mechanistic insights will enable the development of a viable and economical technology for safe water reuse.

KEYWORDS: *wastewater reclamation, hypochlorous species, H_2O_2, reaction kinetics, molecular dynamics, quantum chemistry calculations*

INTRODUCTION

Water reuse plays a vital role in achieving social sustainability, offering a reliable and effective solution to alleviate inadequate access to safe water and water scarcity. Water reuse typically refers to the process of using treated wastewater for beneficial purposes (e.g., landscape irrigation and agricultural processes).[1] Among various viable and economical sources, municipal wastewater effluent is thought to be the most desired due to its massive quantity and steady discharge.[2] Although the effluent can be discharged to surface waters after an activated sludge process and sedimentation, the reclamation of water at this level of quality is restricted due to the presence of harmful bacteria/pathogens and residual organics.[3] Therefore, stringent demands on wastewater treatment have gradually increased over time for water reuse.

Hydroxyl radical ($OH^\bullet$)-based advanced oxidation technologies (AOTs) are able to remove organic pollutants and control pathogenic microorganisms, and they are considered an effective way to improve the quality of reclaimed water.[4,5] The benchmark AOT is the combination of ultraviolet (UV) light and hydrogen peroxide (H_2O_2), an inexpensive and readily available chemical.[6,7] The photochemical formation of $OH^\bullet$ from H_2O_2 is triggered by UV irradiation.[8] However, the UV molar extinction coefficient (ε) of H_2O_2 is remarkably low (19.6 M^{-1} cm^{-1} at 254 nm),[9] indicating that UV irradiation is inefficient in initiating the $OH^\bullet$ formation reaction. This unique drawback/pitfall suggests that a rather high concentration of H_2O_2 would be required to generate a sufficient level of $OH^\bullet$ in engineering practices. This would result in the accumulation of H_2O_2 in treated water, often to an unacceptable level. The residual H_2O_2 needs to be removed, as it is a relatively stable chemical with a half-life of up to multiple days;[10] it also interferes with the determination of the chemical oxygen demand (COD, the most paramount parameter for treatability evaluation) by masking titration

end points.[11,12] In addition, residual H_2O_2 poses toxicity risks due to its high oxidation capabilities. It impairs cellular integrity by damaging cell membranes and proteins, thereby disrupting cell structure and functions.[13,14]

The oxidation of H_2O_2 by hypochlorous species has long been exploited due to the high reactivity and quick kinetics when H_2O_2 is in excess of stoichiometry.[15] It also possesses excellent broad-spectrum disinfectant characteristics toward bacteria and viruses, making it an outstanding choice for disinfection purposes.[16] Therefore, the implementation of hypochlorous species into engineered water treatment systems brings great advantages and acceptability for water reuse. The overall reactions of H_2O_2 with hypochlorous species (HClO and ClO^-) are as follows:

$$H_2O_2 + HClO \rightarrow H_2O + Cl^- + H^+ + O_2 \qquad (1)$$

$$H_2O_2 + ClO^- \rightarrow H_2O + Cl^- + O_2 \qquad (2)$$
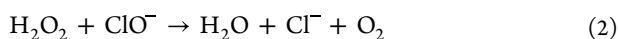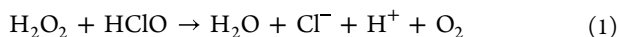
While many studies have investigated the reaction kinetics, the reported rate constants (k; all k values and related nomenclature in this study are listed in Table 1) are widely

Table 1. Rate Constants Related to the Reactions of H_2O_2 with Hypochlorous Species[a]

parameters	note and unit
k_{bi}	bimolecular pathway rate constant, $M^{-1}\,s^{-1}$
k_{tri}	trimolecular pathway rate constant, $M^{-2}\,s^{-1}$
$k_{2,overall}$	second-order overall rate constant for ClO^- and H_2O_2, $M^{-1}\,s^{-1}$
$k'_{2,overall}$	apparent first-order overall decay rate of ClO^-, s^{-1}
k_1	second-order rate constant for HClO and H_2O_2, $M^{-1}\,s^{-1}$
k'_1	apparent first-order decay rate of HClO, s^{-1}
k_{mix}	mixed second-order rate of H_2O_2 with HClO and ClO^-, $M^{-1}\,s^{-1}$

[a]Note that $k_{2,overall}$ was fitted based on a second-order reaction kinetics assumption (i.e., the reaction only follows second-order kinetics), and linear fitting of the slope of $k'_{2,overall}$ with different concentrations of H_2O_2 yields $k_{2,overall}$.

scattered. Held et al. studied the kinetics of H_2O_2 with ClO^- by measuring the primary product singlet molecular oxygen ($^1O_2$) using the chemical trapper 2,5-dimethylfuran.[17] The k value was reported to be $3.4 \times 10^3\ M^{-1}\,s^{-1}$ at a pH of 9.2 and an ionic strength (I) of 0.1 M. By measuring the kinetics of the O_2 build-in reaction using a gasometrical technique, Shams El Din and Mohammed estimated the k value to be less than 10 $M^{-1}\,s^{-1}$ ($I = 0.06$ M).[18] This value is 2 orders of magnitude lower than that determined by Held et al. The discrepancy is even more pronounced for the reaction with HClO. Shishido et al. investigated the reaction kinetics using a competition kinetics method with monochlorodimedone as a reference compound at pH = 7.0 and $I = 0.05$ M.[19] The k value was determined to be $\sim 2 \times 10^5\ M^{-1}\,s^{-1}$. Surprisingly, the k value reported by Son et al. (0.3–2 $M^{-1}\,s^{-1}$ at pH = 2.5), which was determined by monitoring the disappearance rate of H_2O_2, is 5 orders of magnitude lower than that reported by Shishido et al.[20] In addition, discrepancies in the order of the reaction kinetics have also been reported. While most studies assumed second-order reaction kinetics, Maetzke and Knak Jensen found that water molecules played a decisive role in the reaction between ClO^- and H_2O_2, indicating the existence of a higher order of reaction.[21] The discrepancies in these kinetic studies have created significant barriers for the implementation

of hypochlorous species (overdosing or underdosing) for water reuse.

The underlying mechanisms of H_2O_2 reacting with ClO^- have not yet been elucidated. The controversies specifically lie in the following questions: (1) what is the exact electronic state of the product O_2 ($a^1\Delta_g$ or $X^3\Sigma_g^-$)? A chemiluminescence study indicated that the product O_2 is in a singlet state ($^1O_2$) rather than a ground triplet state ($^3O_2$).[22] However, a theoretical study suggested that both $^1O_2$ and $^3O_2$ were formed for this reaction.[23] (2) Where does the product O_2 come from? Cahill and Taube proposed two possible O_2 generation pathways on the basis of isotopic analysis.[24] Their results showed that the O atoms of the product O_2 comes exclusively from H_2O_2. However, the studies by Shakhashiri et al. and Castagna et al. demonstrated that the two O atoms in the product O_2 each comes from hypochlorous species and H_2O_2, respectively.[22,23] (3) Does this reaction involve free radicals? Lontsi Djimeli et al. proposed a redox reaction between ClO^- and H_2O_2 with the formation of ClO_2^- and H_2O.[25] However, an electron paramagnetic resonance (EPR) study indicated the formation of $OH^\bullet$, as evidenced by a persistent spin trap adduct signal.[23] Answers to these questions about both kinetics and mechanisms are indispensable for securing optimal operation conditions for hypochlorous species and for meeting more stringent requirements in water reclamation.

In this context, this study aims to systematically investigate the kinetics and mechanistic and environmental aspects of the H_2O_2 reactions with hypochlorous species through complementary experimental and theoretical approaches. The reaction kinetics of H_2O_2 with HClO/ClO^- was first investigated by a stopped-flow spectroscopic technique. Both speciation- and equilibrium-based approaches were developed to determine the respective k values for the H_2O_2 reactions with HClO and ClO^-. The reaction mechanisms were elucidated by direct molecular dynamics (MD) trajectory simulations, from which bimolecular and trimolecular reaction pathways were identified. The potential energy surfaces (PESs) for the proposed reaction pathways were mapped out using approximate spin-projected density functional theory (AP-DFT) combined with an analysis of reaction multireferential characters. The impact of the environmental matrix was critically assessed by using two waters having discrete characteristics (i.e., municipal wastewater and ammonium-rich wastewater), as they are commonly seen in wastewater treatment and represent diverse compositions needing attention in engineering practices. These results regarding the kinetics and mechanisms of the H_2O_2 and HClO/ClO^- reactions provide a fundamental basis for a better, more in-depth understanding of the reactions and their implications in the development and optimization of the respective engineered treatment processes for safe water reuse.

■ MATERIALS AND METHODS

Materials. Sodium hypochlorite solution (4–4.99%), sodium phosphate monobasic (Na_2HPO_4, ≥99.0%), sodium phosphate dibasic (NaH_2PO_4, ≥99.0%), and sodium phosphate (Na_3PO_4, 96.0%) were purchased from Sigma-Aldrich, U.S. Hydrogen peroxide (H_2O_2, 30 wt % in H_2O) and sodium thiosulfate ($Na_2S_2O_3$) were purchased from Macklin, China. The exact solution concentrations of H_2O_2 and hypochlorous acids were measured by iodometric titration with $Na_2S_2O_3$.[26,27] All of the solutions were freshly prepared using ultrapure (UP)

water obtained from a water purification system (ZWM-PA1-40, ZOOMWO, China).

Experimental Methods. *Wastewater Collection and Characterization.* Samples of municipal wastewater were collected from the secondary effluent of a municipal wastewater treatment plant (WWTP) in Changsha, China. The plant has a treating capacity of 40 000 m^3 d^{-1}, and it receives sewage from a 50 km^2 residential area with a population of $\sim$600 000. This WWTP employs a modified sequencing batch reactor (MSBR) consisting of an anaerobic/anoxic/oxic (A^2/O) system and a SBR in series. The effluent was poured into a 5 L polyethylene barrel (UP water rinsed) with minimal headspace; then, it was transported to our laboratory within 1 h in an ice-bath cooler. The pretreatment procedure the samples underwent is described in the Supporting Information, Text S1.

Samples of ammonium-rich wastewater were collected from the effluent of a pilot-scale anaerobic ammonium oxidation (anammox) sequencing batch reactor (SBR) process. The SBR is illustrated in Figure S1. The SBR was operated at 37 °C in a steady state for $\sim$160 days, and the hydraulic retention time (HRT) was set to 24 h. The influent of the SBR was purged with N_2/CO_2 (95%/5%) to remove the dissolved oxygen (DO). Each SBR cycle duration was 8 h, and the entire operational cycle included 0.3 h of feeding, 6.5 h of stirring, 1 h of settling, and 0.2 h of discharging. The volumetric exchange rate of the SBR was 25%, which means that in a SBR cycle, 25% of the total water volume was discharged and 25% of fresh influent water was introduced into the system. Both the municipal and ammonium-rich wastewater samples were characterized, and the results are tabulated in Table S1. The analytical processes are described in Text S2.

Kinetics Measurements. A modified stopped-flow spectrometer (SX20, Applied Photophysics, U.K.) was used to investigate the rapid kinetics process for the reaction of H_2O_2 with hypochlorous species (Figure S2). Briefly, this system consisted of liquid and light channels. The liquid channel was able to mix both reactants within 1 ms in a 20 μL mixing cell, while the light channel was used to measure the UV absorbance evolution of the HClO/ClO$^-$ mixture to determine first-order rate constants up to 3000 s^{-1}. Please see the detailed operational procedure in Text S3.

All of the kinetics experiments were performed by monitoring the decay of HClO/ClO$^-$ in the presence of excess H_2O_2 at 23 $\pm$ 2 °C. On the basis of the acid dissociation equilibrium constants for HClO (pK_a = 7.53) and H_2O_2 (pK_a = 11.6), the pH of the sample solution was set to 5.5 and 9.5, respectively, to ensure that HClO (99% at 5.5) or ClO$^-$ (99% at 9.5) was the overwhelmingly dominant species in the solution (see Table S2 and Figure S3, dotted vertical lines). The working solutions were buffered in a 0.1 M phosphate buffer (I = 0.3 M). Our preliminary experiments confirmed that the buffer solutions were optically transparent at the detection wavelengths of HClO/ClO$^-$ (data not shown). The selection of the monitoring wavelength for the reaction was based on the steady-state spectra of the reactants and products. The absorption spectra of hypochlorous species, H_2O_2, and the products at different pH values were measured by a UV–vis spectrophotometer (UV-1780, Shimadzu, Japan). The purpose of the measurement was to locate a suitable wavelength for monitoring the depletion of HClO/ClO$^-$ in the presence of excess H_2O_2 with little or no interference. According to their spectra (Figure S4), the UV absorbance of HClO at pH = 5.5

was measured at a wavelength of 236 nm and that of ClO$^-$ at pH = 9.5 was measured at a wavelength of 292 nm for stopped-flow spectroscopy. Under each condition, kinetic traces were obtained with at least 1 log (i.e., 90%) completion of the reaction.

To obtain the decay kinetics, the kinetics experiments were performed with at least a 10-fold excess of H_2O_2 with respect to HClO/ClO$^-$ (i.e., $[H_2O_2] \geq 10 \times [HClO]_{tot}$). The initial concentration of hypochlorous acid was set to 1.5 mM, and the corresponding series of H_2O_2 concentrations was set to 15, 18, 21, 24 and 27 mM. There were two considerations for the 2-fold variation of the concentration of H_2O_2 (15−27 mM). First, in engineering practices, a typical dosing concentration for H_2O_2 is in the millimolar range. Second, a change of twice the H_2O_2 concentration allows one to obtain a highly differentiated first-order decay rate of ClO$^-$. The apparent rate constant (k') can be determined via

$$-\frac{d[HClO]_{tot}}{dt} = k'[HClO]_{tot} \tag{3}$$

where k' is the apparent decay rate constant in units of s^{-1}, and $[HClO]_{tot}$ is the total concentration of HClO and ClO$^-$ regardless of speciation. The k' values were determined by an exponential fitting of the absorbance versus time:

$$A(t) = A_0 \exp(-k't) + C \tag{4}$$

where $A(t)$ represents the absorbance change during the run, A_0 is the initial absorbance at t_0, and C is the constant of integration. The k' values were measured by averaging 5−15 individual acquisitions at any given $[H_2O_2]$.

Impact of Wastewater Matrix. In order to assess the environmental implications of hypochlorous species on wastewater effluent, we investigated the reaction kinetics in two different wastewater effluents and compared them to the kinetics in UP water. The experiments in both the UP water and the wastewater were carried out under the same conditions except for the pH. The pH of the UP water was adjusted to be identical to that of the different wastewater effluents (i.e., pH = 7.5 for municipal wastewater, and pH = 8.5 for ammonium-rich wastewater) with a phosphate buffer. Note that in a similar study by Lu et al., the effects of the water matrix on the attenuation of hypochlorous species were not investigated.[28]

Computational Methods. *Molecular Dynamics Simulations.* To identify the mechanistic origin for the interaction between H_2O_2 and ClO$^-$ in bimolecular collisions, quasi-classical direct trajectories were calculated to mimic the bimolecular reaction outcomes.[29] The aim was to (i) explore probable reaction pathways and product structures and (ii) capture the gross kinetic features of the reaction. Initial conditions for the bimolecular collision trajectories were set up using the VENUS program.[30,31] Vibrational excitations in the trajectory reactants were sampled using quantum Boltzmann probability distributions:[32]

$$P(n_i) = \exp\left(-\frac{n_i h\nu_i}{k_B T}\right)\left[1 - \exp\left(-\frac{h\nu_i}{k_B T}\right)\right] \tag{5}$$

where ν_i and n_i are the vibrational frequency and quantum number of the ith mode, respectively, and T is the simulation temperature. The reactant had zero-point energy (ZPE) in all vibrational modes, and individual atoms were provided momenta and displacements from equilibrium with random phases for all modes. The rotational energy (E_{rot}) of the

reactant was sampled from a classical Boltzmann distribution. Collision energies (E_{CM} in the center of mass) were added as the relative translational energy in the center-of-mass frame of the two reactants.

To minimize the time spent calculating the reactant approach phase in the trajectories, the trajectories were started with randomly oriented reactants with an initial separation of 8.0 Å between the centers of the masses of the collision partners. At this distance, the long-range ion-induced dipole interaction becomes insignificant. The trajectories were propagated using the Hessian-based method implemented in Gaussian 16[33,34] with the Hessians updated every five steps. The DFT method at the ωB97XD/6-31+G(d,p) level was used for the trajectory calculations due to its good balance between computational accuracy and cost. The step size for the trajectory integration was set to 0.25 amu$^{1/2}$ bohr (which corresponded to 0.4 fs in the trajectory time). This step size was sufficiently small to ensure the conservation of the total energy and momentum throughout the trajectory. The trajectories were terminated upon the formation of an ion–molecule complex or if the separation between the centers of the mass of the products exceeded 10 Å. The trajectories were collected at two different collision energies (i.e., 0.5 and 1.0 eV) in the center-of-mass frame. At each collision energy, the impact parameter b was randomly sampled from 0 to 3.0 Å. The gOpenMol software was use for trajectory visualization.[35] Analysis of the individual trajectories was done with a custom program written for this purpose.[36−39] The detailed molecular dynamics simulation for H_2O_2 and ClO^- is discussed in Text S4.

Quantum Chemistry Calculations. Quantum chemistry calculations were employed to investigate the reaction electronic structures and energies of H_2O_2 with ClO^-.[40] All calculations were performed using the Gaussian 16 program package.[34] The structures were optimized at the ωB97XD/6-31+G(d,p) level of theory, as this method provides a high degree of accuracy and reliability in describing the intermolecular interactions of small molecular systems.[41] To mimic reactions in aqueous solutions, a charge density based solvation mode (SMD) was selected, as it is a commonly used model with high applicability.[42] All energy calculations were then performed at the SMD-ωB97XD/aug-cc-pVQZ level of theory. To validate the functional and basis set, the excitation energy of singlet O_2 was calculated to be 22.95 kcal mol^{-1} using the above method. This result is in good agreement with the measured value (22.5 kcal mol^{-1}).[43] All optimized geometries, stationary minima, and transition states (TSs) were confirmed by vibrational frequency calculations at the same level of theory. All frequencies were positive for the reactants and products, while the TSs had one and only one imaginary frequency that corresponds to the reaction coordinate. Intrinsic reaction coordinate calculations were used to ensure the obtained TSs connected the correct reactants and products.[44]

Since $^1O_2$ is involved in this reaction, a single-reference method such as spin-restricted DFT may not be capable of treating the system with significant multireferential character mixing singlet and triplet states, thus overestimating the energies.[45] This inaccuracy in energies, termed spin contamination, would compromise the PES calculations. To eliminate spin contamination, an approximate spin-projection (AP) method was used to correct for energy errors and ensure a proper description of the reactants, intermediates, TSs, and products:[46,47]

$$E_{corrected} = \frac{E^{BS}\langle S^2\rangle^{HS} - E^{HS}\langle S^2\rangle^{BS}}{\langle S^2\rangle^{HS} - \langle S^2\rangle^{BS}} \tag{6}$$

where E^{BS} and E^{HS} represent the calculated energy of a broken-symmetry (BS) ground state and a high-spin (HS) state, respectively, and $\langle S^2\rangle^{BS}$ and $\langle S^2\rangle^{HS}$ are the average values of the total spin angular momentum operator for the denoted state. Prior to executing energy corrections, all optimized structures were subjected to T_1 diagnostics at the CCSD(T)/aug-cc-pVTZ level of theory to determine whether they suffered from spin contamination.[48−50] A T_1 value greater than 0.02 for a closed-shell system indicates severe multiconfigurational character.

RESULTS AND DISCUSSION

Pathway Exploration. Possible reaction pathways that were identified in the MD trajectories are shown in Scheme 1.

Scheme 1. Reaction Mechanisms of ClO$^-$ with H$_2$O$_2$ via Bimolecular and Trimolecular Pathways^a

(a) bimolecular pathway

(b) trimolecular pathway
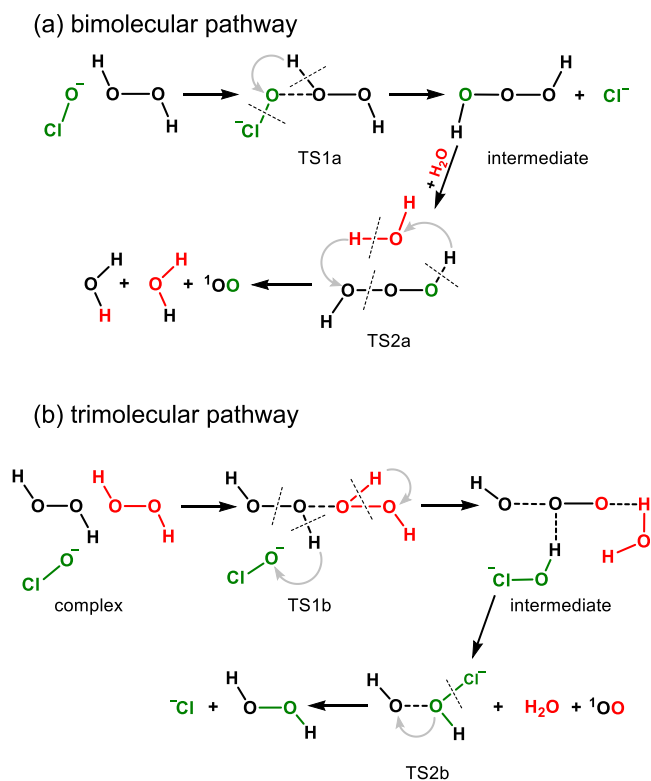
^{a}Different colors are used to track the transfer of atoms in the reaction.

The bimolecular reaction trajectories (Scheme 1a) of H_2O_2 and ClO^- demonstrated that the first step in the reaction is the formation of a trioxidane (HOOOH) intermediate via the transition state TS1a. The trajectory yield for the formation of HOOOH in bimolecular collisions was 3% at an E_{CM} of 0.5 and 1.0 eV. In other words, in all of the trajectories we collected at E_{CM} = 0.5 eV, 3% resulted in the formation of the HOOOH intermediate. The same formation yield for HOOOH was found in the trajectories simulated at E_{CM} = 1.0 eV. The weak energy dependence of the trajectory reaction

yield indicates that the reaction does not require significant energy.

It is well-known that the HOOOH species is unstable (with a half-life of 20 ms) and facilely undergoes decomposition aided by water in aqueous solution.[51,52] To probe the subsequent reaction pathways, various numbers of explicit water molecules were deliberately added around the HOOOH in the PES calculations. It was found that HOOOH may decompose upon a single water ligand, producing $^1O_2$ and two water molecules via TS2a.

In the trimolecular trajectories (Scheme 1b) of two H_2O_2 with ClO^-, the complex $[HOOH \cdot ClO \cdot HOOH]^-$ was formed immediately. The simulation results indicated that the majority of the trajectories of this complex converted to a $H_2O \cdot OO \cdot [ClOH \cdots OH]^-$ intermediate via TS1b. The latter intermediate may decompose to form H_2O, $^1O_2$, and $[ClOH \cdots OH]^-$. The resulting $[ClOH \cdots OH]^-$ subsequently decomposes to Cl^- and H_2O_2 via TS2b. Another minor transformation pathway (accounting for 17% of the trajectories) of the complex $[HOOH \cdot ClO \cdot HOOH]^-$ corresponds to its thermal decomposition to HOOOH, Cl^-, and H_2O_2 (not shown in Scheme 1b due to a similar reaction pattern in the bimolecular pathway).

Kinetics Measurements. *Speciation-Based Approach.* The apparent rate constants (k', s^{-1}, regardless of pathways and speciation) for H_2O_2 reacting with hypochlorous species under different pH conditions are tabulated in Table 2. The k' at any given H_2O_2 concentration increased with an increase in pH, indicating that the speciation of the reacting species in the solution changed with the pH. Figure S3 illustrates that the

dominating species of hypochlorous species was HClO at pH = 5.5 and ClO^- at pH = 9.5. At any given $[H_2O_2]$, the k at pH = 9.5 was approximately 2 orders of magnitude greater than that at pH = 5.5, which simply suggests that the reactivity between H_2O_2 and HClO was rather weak. The reaction between HClO and HO_2^- was not included, as the concentration of HO_2^- was extremely low (<1% at pH = 9.5).

Based on the MD simulations, the overall reaction of ClO^- and H_2O_2 consists of a bimolecular pathway and a trimolecular pathway:

$$ClO^- + H_2O_2 \overset{k_{bi}}{\rightarrow} Cl^- + H_2O + O_2 \tag{7}$$

$$ClO^- + H_2O_2 + H_2O_2 \overset{k_{tri}}{\rightarrow} H_2O_2 + H_2O + Cl^- + O_2 \tag{8}$$
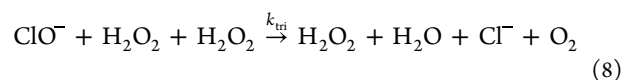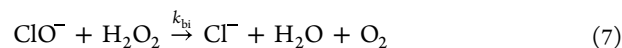
where k_{bi} and k_{tri} denote the rate constants of ClO^- and H_2O_2 in the bimolecular (M^{-1} s^{-1}) and trimolecular (M^{-2} s^{-1}) pathways, respectively. Figure 1 illustrates the process of
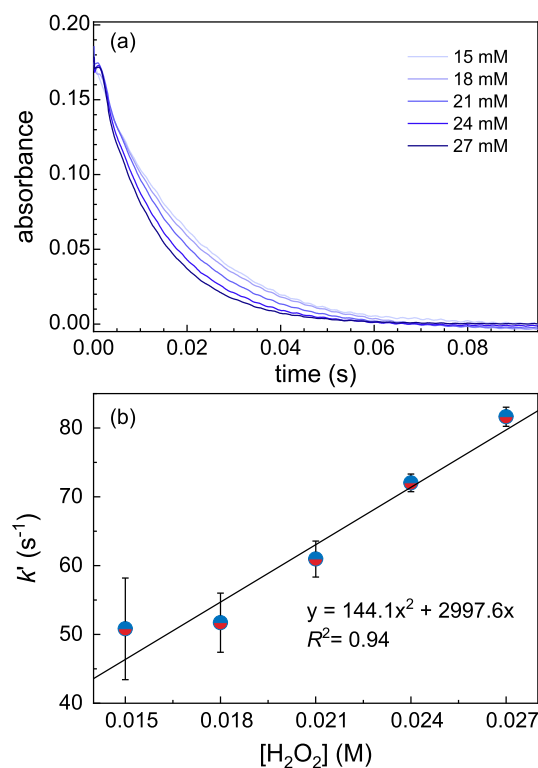
Figure 1. Determining k_{tri} and k_{bi} for the reaction of ClO^- and H_2O_2 by a stopped-flow spectroscopic technique. (a) Decay traces of ClO^- with the H_2O_2 concentration varying from 15 to 27 mM, monitored at a wavelength of 292 nm; (b) Plot of the apparent decay rate versus the H_2O_2 concentration. ($[ClO^-]$ = 1.5 mM, [buffer] = 100 mM, pH = 9.5, and T = 22.8 °C. The mixed blue and red symbols in (b) represent that this reaction is a mix of bimolecular and trimolecular pathways.)

Table 2. Apparent Rate Constants (k', s^{-1}) and Mixed Second-Order Rate Constants (k_{mix}, M^{-1} s^{-1}) for H_2O_2 Reacting with Hypochlorous Species under Different Conditions (Concentrations Given in mM)

pH	[ClO]$_{tot}$	[H$_2$O$_2$]	k'	k_{mix}
5.5	1.5	15	0.738 ± 0.003	42.89 ± 10.8
		18	1.083 ± 0.004	
		21	1.058 ± 0.023	
		24	1.200 ± 0.004	
		27	1.346 ± 0.003	
6.5	1.5	15	4.661 ± 0.031	225.7 ± 30.2
		18	5.520 ± 0.036	
		21	6.164 ± 0.019	
		24	7.196 ± 0.025	
		27	8.163 ± 0.030	
7.5	1.5	15	19.62 ± 0.079	2016 ± 313.0
		18	32.76 ± 0.079	
		21	37.73 ± 0.092	
		24	42.28 ± 0.155	
		27	46.19 ± 0.152	
8.5	1.5	15	41.01 ± 0.041	2781 ± 75.2
		18	48.31 ± 0.047	
		21	56.31 ± 0.070	
		24	64.69 ± 0.091	
		27	74.01 ± 0.106	
9.5	1.5	15	50.82 ± 0.093	2747 ± 325.3
		18	51.71 ± 0.071	
		21	60.95 ± 0.079	
		24	72.02 ± 0.106	
		27	81.64 ± 0.142	

determining k_{tri} and k_{bi} for the reaction of ClO^- and H_2O_2 by stopped-flow spectrometry at pH = 9.5. The traces in Figure 1a show that ClO^- was quickly consumed within 0.05 s. The decay rate of ClO^- increased from 50 to 81 s^{-1} with an increase in $[H_2O_2]$. All of the kinetic traces were well fitted by eq 4, and the k_{tri} and k_{bi} were determined:

$$k' = k_{tri}[H_2O_2]^2 + k_{bi}[H_2O_2] \tag{9}$$

Figure 1b demonstrates the nonlinear fitting between k' and $[H_2O_2]$ via eq 9, and the goodness of fit (R^2) is 0.94. The k_{tri} and k_{bi} values were determined to be $1.44_{-0.7}^{+0.7} \times 10^2$ M^{-2} s^{-1} and $3.00_{-0.13}^{+0.39} \times 10^3$ M^{-1} s^{-1}, respectively. Note the intercept of eq 9 was zero when the best R^2 value was achieved. This result aligns with the fact that the reaction does not occur in the absence of H_2O_2. The k' value at 0.015 M is above the fitted line but still in the error range.

Although k values for the reaction between ClO$^-$ and H_2O_2 have been reported, these values were empirically based on a second-order reaction kinetics assumption. Because different orders of kinetics were not considered in these previous studies,[17,18] a wide range of k values were reported. The measured overall rate constant $(k_{2,overall})$ in our system is in good agreement with those reported in literature (3.4×10^3 M^{-1} s^{-1} by Held et al.[17] and 3.5×10^3 M^{-1} s^{-1} by Lu et al.),[28] ensuring the accuracy and precision of our method. It should be noted that our study represents an attempt to determine pathway-dependent reaction kinetics for the first time. At low concentrations of H_2O_2, the bimolecular pathway dominates the reaction, and $k_{2,overall}$ may well represent the reaction kinetics. At high concentrations of H_2O_2, the trimolecular pathway dominates; thus, it is evident that $k_{2,overall}$ does not truly describe the reaction kinetics of ClO$^-$ and H_2O_2.

In order to understand the reactivity of H_2O_2 with hypochlorous species, the reaction kinetics of H_2O_2 with HClO were also measured at pH = 5.5. Although the fraction of ClO$^-$ accounts for 1% compared to 99% for HClO at pH = 5.5, the contribution of ClO$^-$ to the consumption of H_2O_2 is not negligible on the basis that the reactivity of ClO$^-$ is significantly higher than that of HClO. Meanwhile, the contribution of H_2O_2 depletion to the absorbance change can be neglected, as the ε of HClO is three times higher than that of H_2O_2. Therefore, the absorbance evolution at 236 nm can be attributed to both ClO$^-$ and HClO, and thus, k_1' can be derived from

$$A = A_1 \exp(-k_1't) + A_2 \exp(-k_{2,overall}'t) \tag{10}$$

where A_1 is absorbance of HClO (2.19×10^{-2}) and A_2 is absorbance of ClO$^-$ (2.9×10^{-5}) monitored at the wavelength of 236 nm. These absorbance values correspond to the HClO and ClO$^-$ concentrations of 2.19×10^{-4} and 2.41×10^{-6} M, respectively. $k_{2,overall}'$ is the apparent overall decay rate of ClO$^-$ and can be calculated by

$$k_{2,overall}' = k_{2,overall}[H_2O_2] \tag{11}$$

where $k_{2,overall}$ is the overall rate constant (2746.7 ± 325.3 M^{-1} s^{-1}) of the reaction between H_2O_2 and ClO$^-$. Table S3 lists the k_1' values that were obtained at different concentrations of H_2O_2, and the slope of the line obtained by plotting these k_1' values against $[H_2O_2]$ (i.e., k_1 for the reaction between H_2O_2 and HClO) was determined to be 42.3 ± 13.5 M^{-1} s^{-1} (Figure S5). The k_1 measured in this study was extremely low, which is consistent with the reported values (e.g., 2.0 M^{-1} s^{-1} by Son et al.).[20]

Equilibrium-Based Approach. Because the reported kinetics for the reaction of H_2O_2 with HClO/ClO$^-$ varied by orders of magnitude, we also employed equilibrium-based techniques to measure k_1 and $k_{2,overall}$ to corroborate the speciation-based measurements. In the speciation-based approach, the kinetics were determined at a certain pH condition where only one species dominated the system (i.e.,

9.5 for ClO$^-$ and 5.5 for HClO). In the equilibrium-based approach, the kinetics was determined at any pH condition, and the k value was deduced from the equilibrium constants of HClO and H_2O_2. According to the pK_a equilibrium constants for HClO and H_2O_2, there are four potential species (i.e., HClO, ClO$^-$, H_2O_2, and HO$_2^-$) and four possible types of reactions (i.e., ClO$^-$ + H_2O_2, HClO + H_2O_2, ClO$^-$ + HO$_2^-$, and HClO + HO$_2^-$). The total consumption of hypochlorous species is dependent on the contributions of these four possible reactions. Therefore, a rate law can be formulated:

$$-\frac{d[HClO]_{tot}}{dt} = k_{mix}[HClO]_{tot}[H_2O_2]_{tot}$$
$$= k_{mix}([HClO] + [ClO^-])([H_2O_2] + [HO_2^-]) \tag{12}$$

where k_{mix} is the mixed rate constant for H_2O_2 reacting with HClO and ClO$^-$; the values are tabulated in Table 2. At any pH, the ratio of HClO to ClO$^-$ is dependent on K_2 (Table S2) and the pH:

$$[ClO^-]/[HClO] = K_2/[H^+] \tag{13}$$

Similarly, the ratio of H_2O_2 to HO$_2^-$ is dependent on K_3 (Table S2) and the pH:

$$[HO_2^-]/[H_2O_2] = K_3/[H^+] \tag{14}$$

Using eqs 13 and 14, eq 12 can be rewritten as a function of [HClO] and $[H_2O_2]$

$$-\frac{d[HClO]_{tot}}{dt} = k_{mix}\left([HClO] + \frac{K_2}{[H^+]}[HClO]\right)$$
$$\times \left([H_2O_2] + \frac{K_3}{[H^+]}[H_2O_2]\right)$$
$$= k_{mix}\left(\frac{[H^+] + K_2}{[H^+]}\right)\left(\frac{K_3 + [H^+]}{[H^+]}\right)[HClO][H_2O_2] \tag{15}$$

or as a function of $[ClO^-]$ and $[H_2O_2]$

$$-\frac{d[HClO]_{tot}}{dt} = k_{mix}\left(\frac{[H^+] + K_2}{K_2}\right)\left(\frac{K_3 + [H^+]}{[H^+]}\right)[ClO^-][H_2O_2] \tag{16}$$

Because HO$_2^-$ only accounted for 0.99% at the highest tested pH, we only investigated the reactions of HClO/ClO$^-$ with H_2O_2.

Here, two hypotheses were tested. (i) If eq 1 is the dominant reaction in the system, the total consumption of hypochlorous species can be simplified to

$$-\frac{d[HClO]_{tot}}{dt} = -\frac{d[HClO]}{dt} = k_1[HClO][H_2O_2] \tag{17}$$

With the combination of eqs 15 and 17, equilibrium-based k_1 can be derived:

$$k_1 = k_{mix}\left(\frac{[H^+] + K_2}{[H^+]}\right)\left(\frac{K_3 + [H^+]}{[H^+]}\right) \tag{18}$$

(ii) If eq 2 is the dominant reaction in the system, the total consumption of hypochlorous species can be simplified to

$$-\frac{d[HClO]_{tot}}{dt} = -\frac{d[ClO^-]}{dt} = k_{2,overall}[ClO^-][H_2O_2] \tag{19}$$

With the combination of eqs 16 and 19, equilibrium-based $k_{2,overall}$ can be derived:

$$k_{2,overall} = k_{mix} \left(\frac{[H^+] + K_2}{K_2} \right) \left(\frac{K_3 + [H^+]}{[H^+]} \right) \quad (20)$$

Thus, plugging the k_{mix} values from Table 2 into eqs 18 and 20 gives equilibrium-based k_1 and $k_{2,overall}$ at different pH values (Figure 2a circles and triangles, respectively). For comparison, the k_{mix} values at various pH are also plotted in Figure 2a (bar) as well.
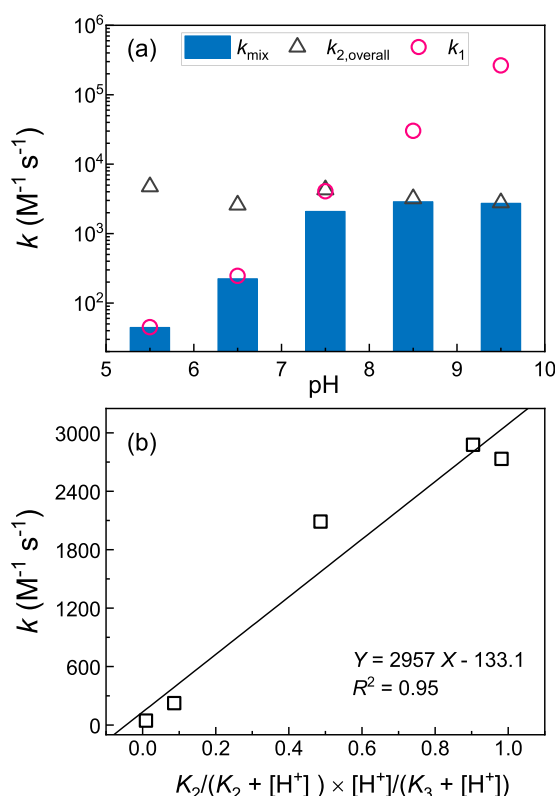
Figure 2. (a) The pH dependence of the rate constants for the reaction of H_2O_2 with HClO (k_1), ClO⁻ ($k_{2,overall}$), and HClO/ClO⁻ (k_{mix}). $k_{2,overall}$ is derived from K_2 and K_3 by $k_{2,overall} = k_{mix} \times ([H^+] + K_2)/K_2 \times ([H^+] + K_3)/[H^+]$. The error bars are smaller than the symbol size and are thus invisible. (b) Plot of the apparent rate constant (k_{mix}, M⁻¹ s⁻¹) against the product of the relative proportion of H_2O_2 to ClO⁻. The slope of the linearly fit line is the value of equilibrium-based $k_{2,overall}$.

Figure 2a illustrates that the equilibrium-based $k_{2,overall}$ values (triangles) are almost constant, indicating its pH-independent characteristic. At pH = 9.5, k_{mix} and equilibrium-based $k_{2,overall}$ completely overlapped. Thus, hypothesis (ii), in which eq 2 is the predominant pathway for hypochlorous species consumption, is supported. According to eq 20, a plot of k_{mix} against $1/\left[\left(\frac{[H^+] + K_2}{K_2} \right) \left(\frac{K_3 + [H^+]}{[H^+]} \right) \right]$ yields $k_{2,overall}$ (i.e., the slope of the line in Figure 2b) with a value of 2957 M⁻¹ s⁻¹, which is consistent with the speciation-based $k_{2,overall}$ value (2997.56 M⁻¹ s⁻¹). Therefore, it is highly convincing that the speciation-based $k_{2,overall}$ value, which we measured via a stopped-flow spectroscopic method, reached the best accuracy.

Unlike $k_{2,overall}$ (triangles in Figure 2a), k_1 (circles) increased with an increase in pH. As the pH increased to 5.5,

equilibrium-based k_1 (44.9 M⁻¹ s⁻¹) exhibited an agreement with the speciation-based k_1 value (42.3 ± 13.5 M⁻¹ s⁻¹). However, with further increases in pH, the equilibrium-based k_1 value was noticeably overestimated. For example, when pH > 6, this value was at least twice that of speciation-based k_1, exceeding the experimental error. Thus, hypothesis (i), in which eq 1 is the predominant pathway for HClO/ClO⁻ consumption, is rejected.

Reaction Mechanisms. *T_1 Diagnostics and Solvation Effect.* Table 3 tabulates the results for $\langle S^2 \rangle$ and T_1 diagnostics

Table 3. $\langle S^2 \rangle$ and T_1 Diagnostics of Wave Functions for the Species Involved the Potential Energy Surfaces[a]

species	$\langle S^2 \rangle$ before	$\langle S^2 \rangle$ after	T_1 diagnostics
H_2O_2	0	0	0.01179
OCl⁻	0	0	0.01659
H_2O	0	0	0.00931
$^1O_2$	1.0039	0.0313	0.01515
$^3O_2$	2.0093	2.0000	0.01758
Bimolecular Pathway			
[ClO·HOOH]⁻	0	0	0.01426
TS1a	0.1804	0.0008	0.02826
[HOOOH·Cl]⁻	0	0	0.01433
HOOOH	0	0	0.01591
TS2a	0	0	0.02447
Trimolecular Pathway			
[HOOH·ClO·HOOH]⁻	0	0	0.01387
TS1b	0	0	0.02622
$H_2O·O_2·[ClOH \cdots OH]^-$	0	0	0.01662
TS2b	0	0	0.02752

[a]The $\langle S^2 \rangle$ and T_1 diagnostics were calculated at ωB97XD/6-31+G(d,p) and CCSD(T)/aug-cc-pVTZ, respectively.

calculated at the ωB97XD/6-31+G(d,p) and CCSD(T)/aug-cc-pVTZ levels of theory, respectively. The results show that four TS species in the bimolecular and trimolecular pathways (Scheme 1) have T_1 values slightly exceeding 0.02. Thus, the energies of the TSs should be corrected for spin contamination. The $\langle S^2 \rangle$ values of bimolecular TS1a are greater than 0 before and after the annihilation of spin contamination, indicating the reliability of the $\langle S^2 \rangle$ values. In contrast, the remaining three TS structures have a $\langle S^2 \rangle$ value of 0, indicating the $\langle S^2 \rangle$ test was less robust for these structures. Based on the $\langle S^2 \rangle$ values, we used the multiconfigurational method CASSCF (complete active space self-consistent field) to obtain a more accurate single-point energy for the three spin-contaminated TS species.

The $\Delta^{\ddagger}G°$ values of TS1a/b for the bimolecular and trimolecular pathways (Scheme 1) were calculated to be 21.3 and 24.0 kcal mol⁻¹, respectively. However, these energy barriers for these two pathways are extremely high, resulting in low k values using the Arrhenius equation (less than 10^{-5} M⁻² s⁻¹ or M⁻¹ s⁻¹, detailed in Text S5). Therefore, we suspected that the low k value may be attributed to the lack of consideration of the solvent effect.[53,54] In order to elucidate the solvent-involved mechanisms for the reaction between H_2O_2 and ClO⁻, we used the quantum chemistry method to identify an appropriate number of water ligands. Figure S6 illustrates the effect of explicit water molecules on the activation barrier ($\Delta^{\ddagger}G°$) of TS1a/b in both pathways. The calculated $\Delta^{\ddagger}G°$ values decrease as the number of water

molecules increases from zero to three; then, they remain unchanged with an increase from three to four water molecules. The correlation between the TS free energy and the number of explicit water ligands suggests that the first three water molecules are most likely located within the first solvation shell of the reacting species and influence the reaction energy directly, whereas additional water molecules become less important to the reaction.

Bimolecular Pathway. The PES for the bimolecular pathway (Scheme 1a) with three explicit water molecules is illustrated in Figure 3a. The bimolecular pathway is initiated by
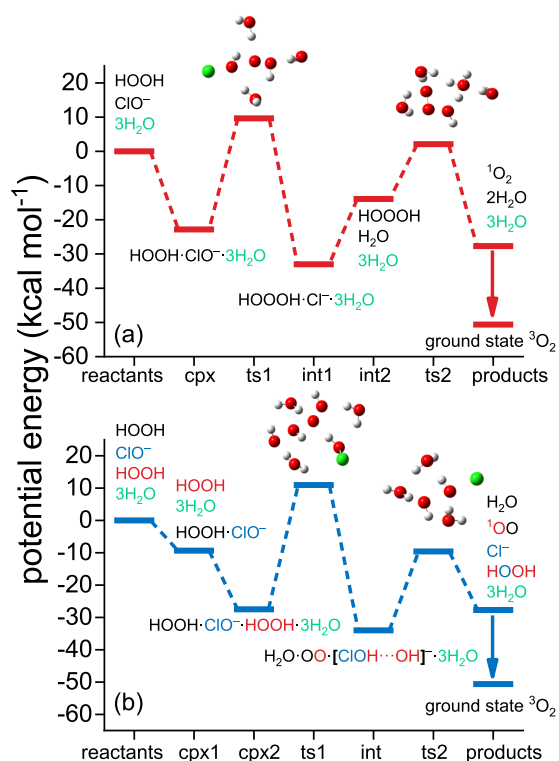
Figure 3. Reaction PES for ClO^- with H_2O_2 via the (a) bimolecular pathway and (b) trimolecular pathway at the ωB97XD/augcc-pVQZ//ωB97XD/6-31+G(d,p) level of theory with the SMD model.

the formation of a pre-reaction hydrogen-bonded complex $[HOOH\cdot ClO]^-$ with a Gibbs free energy $(\Delta_r G^\circ)$ value of -9.33 kcal mol^{-1}. Subsequently, the H atom of HOOH approaches the O atom of ClO^-, and the newly formed OH moiety of ClOH vibrates between the Cl atom and the HOO moiety at TS1a. The rearrangement at TS1a leads to the formation of HOOOH and the elimination of Cl^-:

$$[HOOH\cdot ClO]^- \rightarrow HOOOH + Cl^- \tag{21}$$
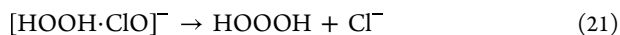
The $\Delta^\ddagger G^\circ$ of TS1a was calculated to be 9.65 kcal mol^{-1}, which is approximately 30 kcal mol^{-1} lower than the $\Delta^\ddagger G^\circ$ reported in the literature.[28] Lu et al. depicted the reaction PES between H_2O_2 and ClO^- based on the bimolecular reaction pathway (the trimolecular pathway was not considered). They proposed the same first step for the formation of HOOOH, and they calculated $\Delta^\ddagger G^\circ$ to be 39.8 kcal mol^{-1} using the B3LYP/6-311+G(d,p) level of theory. It appears that the $\Delta^\ddagger G^\circ$ value is high, indicating that this reaction is kinetically slow. Their disagreement between their theoretical and measured k (in their case, 3.5×10^3 M^{-1} s^{-1}) could be due to the lack of consideration of the multireference characters for the spin-

contaminated species ($^1O_2$ and HOOOH) and the impact of explicit water molecules on TS species. We calculated the k value of the bimolecular pathway with Arrhenius equation (Text S5), and the theoretical k_{bi} was determined to be 1.22×10^3 M^{-1} s^{-1}. We used a pre-exponential factor A of 1.33×10^{10} M^{-1} s^{-1} based on the study by Connick for the same reaction system.[55] Note the A value is close to the theoretical one from collision theory.[55] This k_{bi} value is in reasonable agreement with our measured one (3.00×10^3 M^{-1} s^{-1}), validating the proposed bimolecular pathway.

For TS2a, water molecules acting as H atom passengers participate in the rearrangement of the HOOOH moiety (Scheme 1a). The OH bond in H_2O and the OH bond in HOOOH break simultaneously. The exchange of H atoms between H_2O and HOOOH leads to the cleavage of HOOOH and the formation of another H_2O and $^1O_2$:

$$HOOOH \xrightarrow{H_2O} H_2O + {}^1O_2 \tag{22}$$
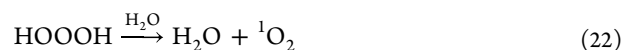
The H_2O molecule acts as a catalyst and decreases the energy barrier. The $\Delta^\ddagger G^\circ$ of TS2a was calculated to be 15.9 kcal mol^{-1}, which is 21.1 kcal mol^{-1} lower than the value reported by Maetzke and Knak Jensen.[21] The abnormally high $\Delta^\ddagger G^\circ$ in their study may be attributed to the lack of consideration of the catalytic role of water molecules.

Trimolecular Pathway. The PES for the trimolecular pathway (Scheme 1b) with three explicit water molecules is illustrated in Figure 3b. Our DFT results indicated that the first step in this pathway is the formation of a hydrogen-bonded complex $[HOOH\cdot ClO]^-$ (eq 23), which is the same as the first step in the bimolecular pathway. The pre-reaction complex then attracts another HOOH to form the more stable complex $[HOOH\cdot ClO\cdot HOOH]^-$, which has a $\Delta_r G^\circ$ value of -27.5 kcal mol^{-1} (eq 24):

$$HOOH + ClO^- \rightarrow [HOOH\cdot ClO]^- \tag{23}$$

$$[HOOH\cdot ClO]^- + HOOH \rightarrow [HOOH\cdot ClO\cdot HOOH]^- \tag{24}$$
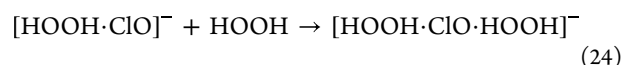
Subsequently, the complex anion is subjected to rearrangement via TS1b. The cleavage of one HOOH leads to the elimination of H_2O, and the remaining O atom moves onto another HOOH, extracting an O to form $^1O_2$ (eq 25):

$$ClO^- + HOOH + HOOH \rightarrow [ClOH\cdots OH]^- + H_2O + {}^1O_2 \tag{25}$$
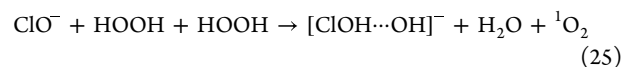
Note that in the trimolecular pathway, the two O atoms of $^1O_2$ come from one H_2O_2 molecule, whereas in the bimolecular pathway, one of the two O atoms comes from H_2O_2 and the other comes from ClO^-. The resulting $^1O_2$ decays to $^3O_2$ regardless of the pathway, validating a previous literature report that both $^1O_2$ and $^3O_2$ are present in this reaction.[23] In eq 25, the remaining part of HOOH after the extraction of an O atom combines with ClO^- to form the intermediate $[ClOH\cdots OH]^-$ (Figure 3b). The OH in $[ClOH\cdots OH]^-$ can be used to support that $OH^\bullet$ was generated and detected by EPR by Castagna et al.[23] The second HOOH molecule acts as a catalyst, significantly reducing $\Delta^\ddagger G^\circ$ for this pathway. The $\Delta^\ddagger G^\circ$ for TS1b was calculated to be 10.9 kcal mol^{-1}. We then calculated the k value of TS1b by using the Arrhenius equation (Text S5), and the k_{tri} was determined to be 136 M^{-2} s^{-1} (note that k_{tri} measured by stopped-flow spectroscopy was 144 M^{-2} s^{-1}). The agreement of the calculated and measured k_{tri} values corroborate the proposed trimolecular pathway. It should be

noted that this is the first time that the trimolecular pathway is reported.

Then, the intermediate $[ClOH\cdots OH]^-$ is subject to rearrangement via TS2b, where the OH moiety of ClOH swings between Cl^- and another OH. The two OH moieties recombine and ultimately form a new HOOH molecule:

$$[ClOH\cdots OH]^- \rightarrow HOOH + Cl^- \quad (26)$$
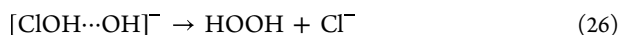
This step was also calculated to be thermodynamically favorable with a $\Delta_r G°$ of -0.58 kcal mol^{-1}.

Environmental Implications. In order to evaluate the feasibility of using hypochlorous species for the removal of H_2O_2 residuals in reclaimed waters, we compared the kinetics in different water matrices. Figure 4a demonstrates that the
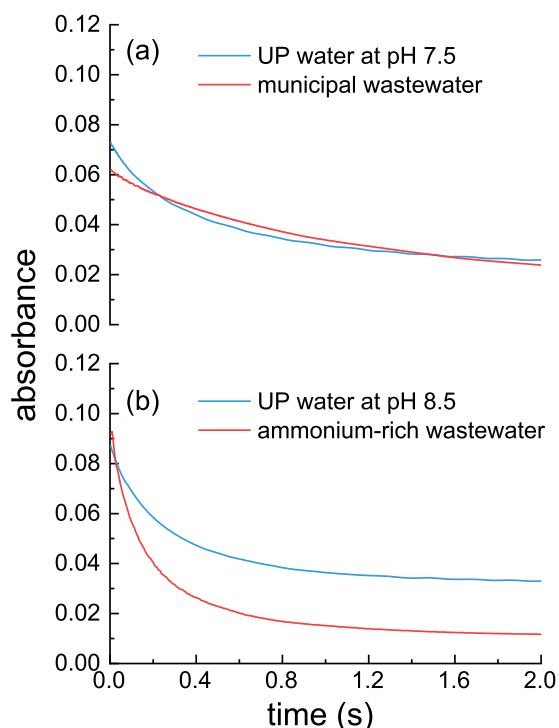
Figure 4. Impact of (a) municipal wastewater and (b) ammonium-rich wastewater on the reaction kinetics of hypochlorous species with H_2O_2 ([H_2O_2] = 1 mM, [hypochlorous species] = 1.5 mM, [buffer] = 100 mM).

decay processes of hypochlorous species in both UP water and municipal wastewater effluents are quite similar. This similarity indicates that the presence of the municipal wastewater matrix exhibits limited effect on the reaction. However, Figure 4b illustrates that at pH = 8.5, ClO^- monitored at 292 nm decreases much faster in ammonium-rich wastewater than in UP water. Within the initial 0.4 s, the consumption of hypochlorous species in ammonium-rich wastewater was about 80%, which was twice as much as that in UP water. This discrepancy in the decay kinetics can be mainly attributed to the competition of ammonia and nitrite for H_2O_2. Weil and Morris investigated the reaction kinetics between HClO and NH_3 using a colorimetric technique, allowing them to follow the progress of the reaction.[56] They reported that hypochlorous species reacted rapidly with ammonia to form monochloramine (NH_2Cl), dichloramine ($NHCl_2$), or trichloramine (NCl_3):

$$NH_3 + HClO \rightarrow NH_2Cl + H_2O \quad (27)$$

$$NH_2Cl + HClO \rightarrow NHCl_2 + H_2O \quad (28)$$

$$NHCl_2 + HClO \rightarrow NCl_3 + H_2O \quad (29)$$
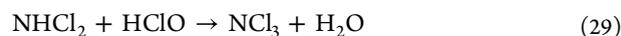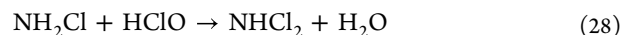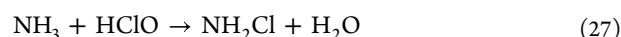
Note the products (chloramines) of these reactions do not exhibit significant absorbance at 292 nm,[57] and thus, they do not interfere with the decay of ClO^- (Figure 4b). When the stoichiometric ratio of HClO to NH_3 is lower than 1:1, NH_2Cl forms rapidly (eq 27), and the k value of the reaction was determined to be 5.6×10^6 M^{-1} s^{-1}.[56] In addition, Lahoutifard et al. studied the reaction between hypochlorous species and nitrite (NO_2^-) with spectrophotometric measurements.[58] The k value of the reaction was determined to be $(8.0 \pm 0.7) \times 10^3$ M^{-1} s^{-1}. The reported k values of these competitive substrates (i.e., NH_3 and NO_2^-) for hypochlorous species are higher than (or at least comparable to) that of H_2O_2. Table S1 shows that the ammonia and nitrite contents in the municipal wastewater effluent are relatively low (4.52 and 0.37 mg L^{-1}, respectively). In contrast, the ammonium-rich wastewater presents a much higher concentration of NH_3 (50.6 mg L^{-1}) and NO_2^- (71.5 mg L^{-1}). The difference in these wastewaters explains our observation of the matrix-dependent decay kinetics in Figure 4. Therefore, on the basis of this matrix-dependent characterization, it is not recommended to use hypochlorous species as a tertiary treatment process for wastewater reclamation for water that has a high concentration of nitrogenous compounds, such as treated waters from sludge dewatering processes, farrowing pen clean-up, and pharmaceutical manufacturing.[59] In order to reduce the cost of reclaimed water, pretreatment technologies for removing total nitrogen such as ion exchange, membrane filtration, and adsorption are highly recommended to lower the concentrations of ammonia and nitrite to below 10 mg L^{-1}. To ensure a sufficient hypochlorous species residual for disinfection purposes, it is recommended to maintain H_2O_2 concentrations at low concentrations to reduce the rapid consumption of hypochlorous species via the trimolecular pathway. Note that in wastewaters where high doses of H_2O_2 are needed, the trimolecular pathway exerts a substantial influence. For example, palm oil mill effluent has been reported to be highly contaminated with a COD exceeding 8.0×10^4 mg L^{-1}. Manickam et al. used the combination of ultrasound and H_2O_2 technologies to lower the COD in the effluent, and the dose of H_2O_2 in their study was 8.8 M.[60] Further, Guzman et al. applied a photo-Fenton process to treat wastewater from the citrus processing industry with a COD of 2.6×10^4 mg L^{-1}, and the H_2O_2 dose was also high, up to 0.5 M.[61]

H_2O_2-based AOTs have been widely used in municipal and industrial wastewater treatment, while hypochlorous species are extensively used as a disinfectant in potable water and other waters (e.g., swimming pool water and landscape water) that directly contact skin. The present study demonstrates that using the cheap and readily available hypochlorous species as the final treatment unit of the tertiary stage not only provides disinfection benefits but also neutralizes the residual H_2O_2. Based on our results, the simple combination of these two processes gains great practical advantages. First, the combination mitigates additional building units for treating residual H_2O_2, significantly reducing construction costs and amount of required land. Second, we emphasize the novelty that $^1O_2$ and $^3O_2$ can be generated via both bimolecular and trimolecular pathways, and the continuous generation and accumulation of

$^1O_2$ is of practical benefit. The remarkable selective reactivity of $^1O_2$ toward arenes with electron-rich functional groups (e.g., phenols and aromatic amino acids) renders it a highly reactive species for the further reduction of soluble microbial products (SMPs), as their major component consists of phenolic and amino moieties.[62,63] It also exhibits low reactivity toward background organic and inorganic water matrices,[64] allowing for more efficient SMP reduction. In addition, $^1O_2$ also kills cells through oxidatively generated damage to methionine, cysteine, DNA guanine nucleobases, lipids, and other biomolecules.[65] In light of these mature AOT and disinfection operations, there is justification for further assessing the proposed combined technology in full scale applications for the safe reuse of reclaimed water.

ASSOCIATED CONTENT

Supporting Information

The Supporting Information is available free of charge at https://pubs.acs.org/doi/10.1021/acs.est.3c06375.

> Wastewater pretreatment, wastewater characterization, operational procedure for stopped-flow spectroscopy, dynamics simulation results of trimolecular reactions, calculations of reaction rate constants, wastewater characteristics, equilibrium constants for HClO and H_2O_2, the derivation of k_1 based on HClO/ClO$^-$ speciation, the pilot-scale sequencing batch reactor, the modified stopped-flow spectroscopy process, the fraction of different species as a function of pH, UV spectra of HClO and ClO$^-$, plot of k_1' vs $[H_2O_2]$, and plot of $\Delta^{\ddagger}G°$ of bi- and trimolecular pathways vs number of H_2O molecules (PDF)

AUTHOR INFORMATION

Corresponding Authors

Jianbo Liu − *Department of Chemistry and Biochemistry, Queens College of the City University of New York, Queens, New York 11367, United States;* orcid.org/0000-0001-9577-3740; Phone: 1-718-997-3271; Email: jianbo.liu@qc.cuny.edu

Ruiyang Xiao − *Institute of Environmental Engineering, School of Metallurgy and Environment, Central South University, Changsha 410083, China; Chinese National Engineering Research Center for Control and Treatment of Heavy Metal Pollution, Changsha 410083, China;* orcid.org/0000-0001-9516-2202; Phone: +86-731-88830875; Email: xiao.53@csu.edu.cn

Authors

Zonghao Luo − *Institute of Environmental Engineering, School of Metallurgy and Environment, Central South University, Changsha 410083, China; Chinese National Engineering Research Center for Control and Treatment of Heavy Metal Pollution, Changsha 410083, China*

Wenjing Zhou − *Department of Chemistry and Biochemistry, Queens College of the City University of New York, Queens, New York 11367, United States;* orcid.org/0000-0001-6985-0263

Ying Jiang − *Institute of Environmental Engineering, School of Metallurgy and Environment, Central South University, Changsha 410083, China; Chinese National Engineering Research Center for Control and Treatment of Heavy Metal Pollution, Changsha 410083, China*

Daisuke Minakata − *Department of Civil and Environmental Engineering, Michigan Technological University, Houghton, Michigan 49931, United States;* orcid.org/0000-0003-3055-3880

Richard Spinney − *Department of Chemistry and Biochemistry, The Ohio State University, Columbus, Ohio 43210, United States;* orcid.org/0000-0002-8074-3386

Dionysios D. Dionysiou − *Environmental Engineering and Science Program, University of Cincinnati, Cincinnati, Ohio 45221, United States;* orcid.org/0000-0002-6974-9197

Complete contact information is available at:
https://pubs.acs.org/10.1021/acs.est.3c06375

Notes

The authors declare no competing financial interest.

REFERENCES

(1) Cisneros, B. J. The data gap. *Nature* **2013**, *502* (7473), 633−634.

(2) Martín, H. G.; Ivanova, N.; Kunin, V.; Warnecke, F.; Barry, K. W.; McHardy, A. C.; Yeates, C.; He, S.; Salamov, A. A.; Szeto, E.; Dalin, E.; Putnam, N. H.; Shapiro, H. J.; Pangilinan, J. L.; Rigoutsos, I.; Kyrpides, N. C.; Blackall, L. L.; McMahon, K. D.; Hugenholtz, P. Metagenomic analysis of two enhanced biological phosphorus removal (EBPR) sludge communities. *Nat. Biotechnol.* **2006**, *24* (10), 1263−1269.

(3) Shannon, M. A.; Bohn, P. W.; Elimelech, M.; Georgiadis, J. G.; Mariñas, B. J.; Mayes, A. M. Science and technology for water purification in the coming decades. *Nature* **2008**, *452* (7185), 301−310.

(4) Aguas, Y.; Hincapie, M.; Martínez-Piernas, A. B.; Agüera, A.; Fernández-Ibáñez, P.; Nahim-Granados, S.; Polo-López, M. I. Reclamation of real urban wastewater using solar advanced oxidation processes: An assessment of microbial pathogens and 74 organic microcontaminants uptake in lettuce and radish. *Environ. Sci. Technol.* **2019**, *53* (16), 9705−9714.

(5) Gassie, L. W.; Englehardt, J. D. Advanced oxidation and disinfection processes for onsite net-zero greywater reuse: A review. *Water Res.* **2017**, *125*, 384−399.

(6) Zhang, S.; Liu, X.; Wang, M.; Wu, B.; Pan, B.; Yang, H.; Yu, H.-Q. Diketone-mediated photochemical processes for target-selective degradation of dye pollutants. *Environ. Sci. Technol. Lett.* **2014**, *1* (2), 167−171.

(7) Chu, C.; Yan, Y.; Ma, J.; Jin, S.; Spinney, R.; Dionysiou, D. D.; Zhang, H.; Xiao, R. Implementation of laser flash photolysis for radical-induced reactions and environmental implications. *Water Res.* **2023**, *244*, 120526.

(8) Sarathy, S. R.; Mohseni, M. The impact of UV/H_2O_2 advanced oxidation on molecular size distribution of chromophoric natural organic matter. *Environ. Sci. Technol.* **2007**, *41* (24), 8315−8320.

(9) Baxendale, J. H.; Wilson, J. A. The photolysis of hydrogen peroxide at high light intensities. *Trans. Faraday Soc.* **1957**, *53*, 344−356.

(10) Kwan, W. P.; Voelker, B. M. Decomposition of hydrogen peroxide and organic compounds in the presence of dissolved iron and ferrihydrite. *Environ. Sci. Technol.* **2002**, *36* (7), 1467−1476.

(11) Guedes, A. M. F. M.; Madeira, L. M. P.; Boaventura, R. A. R.; Costa, C. A. V. Fenton oxidation of cork cooking wastewater—overall kinetic analysis. *Water Res.* **2003**, *37* (13), 3061−3069.

(12) Aceituno, M.; Stalikas, C. D.; Lunar, L.; Rubio, S.; Pérez-Bendito, D. H_2O_2/TiO_2 photocatalytic oxidation of metol. Identification of intermediates and reaction pathways. *Water Res.* **2002**, *36* (14), 3582−3592.

(13) Deavall, D. G.; Martin, E. A.; Horner, J. M.; Roberts, R. Drug-induced oxidative stress and toxicity. *J. Toxicol.* **2012**, *2012*, 645460.

(14) Sharma, P.; Jha, A. B.; Dubey, R. S.; Pessarakli, M. Reactive oxygen species, oxidative damage, and antioxidative defense mechanism in plants under stressful conditions. *J. Bot.* **2012**, *2012*, 217037.

(15) Wang, C.; Hofmann, M.; Safari, A.; Viole, I.; Andrews, S.; Hofmann, R. Chlorine is preferred over bisulfite for H_2O_2 quenching following UV-AOP drinking water treatment. *Water Res.* **2019**, *165*, 115000.

(16) Wang, J.; Shen, J.; Ye, D.; Yan, X.; Zhang, Y.; Yang, W.; Li, X.; Wang, J.; Zhang, L.; Pan, L. Disinfection technology of hospital wastes and wastewater: Suggestions for disinfection strategy during coronavirus Disease 2019 (COVID-19) pandemic in China. *Environ. Pollut.* **2020**, *262*, 114665.

(17) Held, A. M.; Halko, D. J.; Hurst, J. K. Mechanisms of chlorine oxidation of hydrogen peroxide. *J. Am. Chem. Soc.* **1978**, *100* (18), 5732−5740.

(18) Shams El Din, A. M.; Mohammed, R. A. Kinetics of the reaction between hydrogen peroxide and hypochlorite. *Desalination* **1998**, *115* (2), 145−153.

(19) Shishido, N.; Nakamura, S.; Nakamura, M. Dissociation of DNA double strand by hypohalous acids. *Redox. Rep.* **2000**, *5* (4), 243−247.

(20) Son, H.; Cho, M.; Kim, J.; Oh, B.; Chung, H.; Yoon, J. Enhanced disinfection efficiency of mechanically mixed oxidants with free chlorine. *Water Res.* **2005**, *39* (4), 721−727.

(21) Maetzke, A.; Knak Jensen, S. J. Reaction paths for production of singlet oxygen from hydrogen peroxide and hypochlorite. *Chem. Phys. Lett.* **2006**, *425* (1), 40−43.

(22) Shakhashiri, B. Z.; Williams, L. G. Singlet oxygen in aqueous solution: A lecture demonstration. *J .Chem. Educ.* **1976**, *53* (6), 358.

(23) Castagna, R.; Eiserich, J. P.; Budamagunta, M. S.; Stipa, P.; Cross, C. E.; Proietti, E.; Voss, J. C.; Greci, L. Hydroxyl radical from the reaction between hypochlorite and hydrogen peroxide. *Atmos. Environ.* **2008**, *42* (26), 6551−6554.

(24) Cahill, A. E.; Taube, H. The use of heavy oxygen in the study of reactions of hydrogen peroxide. *J. Am. Chem. Soc.* **1952**, *74* (9), 2312−2318.

(25) Lontsi Djimeli, C.; Tamsa Arfao, A.; Noah Ewoti, O. V.; Nougang, M. E.; Moungang, M. L.; Bricheux, G.; Nola, M.; Sime-Ngando, T. Mixture of sodium hypochlorite and hydrogen peroxide on adhered aeromonas hydrophila to solid substrate in water: Impact of concentration and assessment of the synergistic effect. *Int. J. Bacteriol.* **2014**, *2014*, 121367.

(26) Domínguez-Henao, L.; Turolla, A.; Monticelli, D.; Antonelli, M. Assessment of a colorimetric method for the measurement of low concentrations of peracetic acid and hydrogen peroxide in water. *Talanta* **2018**, *183*, 209−215.

(27) Gordon, G.; Tachiyashiki, S. Kinetics and mechanism of formation of chlorate ion from the hypochlorous acid/chlorite ion reaction at pH 6−10. *Environ. Sci. Technol.* **1991**, *25* (3), 468−474.

(28) Lu, X.; Zhou, X.; Qiu, W.; Wang, Z.; Wang, Y.; Zhang, H.; Yu, J.; Wang, D.; Gu, J.; Ma, J. Kinetics and mechanism of the reaction of hydrogen peroxide with hypochlorous acid: Implication on electrochemical water treatment. *J .Hazard. Mater.* **2022**, *438*, 129420.

(29) Bai, L.; Jiang, Y.; Xia, D.; Wei, Z.; Spinney, R.; Dionysiou, D. D.; Minakata, D.; Xiao, R.; Xie, H.-B.; Chai, L. Mechanistic understanding of superoxide radical-mediated degradation of perfluorocarboxylic acids. *Environ. Sci. Technol.* **2022**, *56* (1), 624−633.

(30) Hu, X.; Hase, W. L.; Pirraglia, T. Vectorization of the general Monte Carlo classical trajectory program VENUS. *J .Comput. Chem.* **1991**, *12* (8), 1014−1024.

(31) Hase, W. L.; Bolton, K.; de Sainte Claire, P.; Duchovic, R. J.; Hu, X.; Komornicki, A.; Li, G.; Lim, K.; Lu, D.; Peslherbe, G. H.; et al. In *VENUS 99: A General Chemical Dynamics Computer Program*; Texas Tech University, Lubbock, Texas, U.S., 1999.

(32) Peslherbe, G. H.; Wang, H.; Hase, W. L. Monte Carlo Sampling for Classical Trajectory Simulations. *Advances in Chemical Physics* **1999**, *105*, 171−201.

(33) Bakken, V.; Millam, J. M.; Bernhard Schlegel, H. Ab initio classical trajectories on the Born−Oppenheimer surface: Updating methods for Hessian-based integrators. *J. Chem. Phys.* **1999**, *111* (19), 8773−8777.

(34) Frisch, M. J.; Trucks, G. W.; Schlegel, H. B.; Scuseria, G. E.; Robb, M. A.; Cheeseman, J. R.; Scalmani, G.; Barone, V.; Petersson, G. A.; Nakatsuji, H.; Li, X.; Caricato, M.; Marenich, A. V.; Bloino, J.; Janesko, B. G.; Gomperts, R.; Mennucci, B.; Hratchian, H. P.; Ortiz, J. V.; Izmaylov, A. F.; Sonnenberg, J. L.; Williams; Ding, F.; Lipparini, F.; Egidi, F.; Goings, J.; Peng, B.; Petrone, A.; Henderson, T.; Ranasinghe, D.; Zakrzewski, V. G.; Gao, J.; Rega, N.; Zheng, G.; Liang, W.; Hada, M.; Ehara, M.; Toyota, K.; Fukuda, R.; Hasegawa, J.; Ishida, M.; Nakajima, T.; Honda, Y.; Kitao, O.; Nakai, H.; Vreven, T.; Throssell, K.; Montgomery, J. A., Jr.; Peralta, J. E.; Ogliaro, F.; Bearpark, M. J.; Heyd, J. J.; Brothers, E. N.; Kudin, K. N.; Staroverov, V. N.; Keith, T. A.; Kobayashi, R.; Normand, J.; Raghavachari, K.; Rendell, A. P.; Burant, J. C.; Iyengar, S. S.; Tomasi, J.; Cossi, M.; Millam, J. M.; Klene, M.; Adamo, C.; Cammi, R.; Ochterski, J. W.; Martin, R. L.; Morokuma, K.; Farkas, O.; Foresman, J. B.; Fox, D. J. In *Gaussian 16 Rev. C.01*; Gaussian, Inc., Wallingford, Connecticut, U.S., 2016.

(35) Laaksonen, L. In *gOpenMol*, 3.0 ed.; Center for Scientific Computing, Espoo, Finland, 2005; Vol. *3.0*.

(36) Liu, J.; Zhou, W.; Chambreau, S. D.; Vaghjiani, G. L. Computational study of the reaction of 1-Methyl-4-amino-1,2,4-triazolium dicyanamide with NO_2: From reaction dynamics to potential surfaces, kinetics and spectroscopy. *J. Phys. Chem. B* **2019**, *123* (13), 2956−2970.

(37) Liu, J.; Zhou, W.; Chambreau, S. D.; Vaghjiani, G. L. Molecular dynamics simulations and product vibrational spectral analysis for the reactions of NO_2 with 1-Ethyl-3-methylimidazolium dicyanamide ($EMIM^+DCA^-$), 1-Butyl-3-methylimidazolium dicyanamide ($BMIM^+DCA^-$), and 1-Allyl-3-methylimidazolium dicyanamide ($AMIM^+DCA^-$). *J. Phys. Chem. B* **2020**, *124* (21), 4303−4325.

(38) Zhou, W.; Liu, J.; Chambreau, S. D.; Vaghjiani, G. L. Molecular dynamics simulations, reaction pathway and mechanism dissection, and kinetics modeling of the nitric acid oxidation of dicyanamide and dicyanoborohydride anions. *J. Phys. Chem. B* **2020**, *124* (49), 11175−11188.

(39) Zhou, W.; Liu, J.; Chambreau, S. D.; Vaghjiani, G. L. Structures, proton transfer and dissociation of hydroxylammonium nitrate (HAN) revealed by electrospray ionization tandem mass spectrometry and molecular dynamics simulations. *Phys. Chem. Chem, Phys.* **2022**, *24* (22), 14033−14043.

(40) Kohn, W.; Sham, L. J. Self-consistent equations including exchange and correlation effects. *Phys. Rev.* **1965**, *140* (4A), A1133−A1138.

(41) Wang, C.; Qiao, Q.; Chi, W.; Chen, J.; Liu, W.; Tan, D.; McKechnie, S.; Lyu, D.; Jiang, X.-F.; Zhou, W.; Xu, N.; Zhang, Q.; Xu, Z.; Liu, X. Quantitative design of bright fluorophores and AIEgens by the accurate prediction of twisted intramolecular charge transfer (TICT). *Angew. Chem., Int. Ed.* **2020**, *132* (25), 10246−10258.

(42) Marenich, A. V.; Cramer, C. J.; Truhlar, D. G. Performance of SM6, SM8, and SMD on the SAMPL1 test set for the prediction of small-molecule solvation free energies. *J. Phys. Chem. B* **2009**, *113* (14), 4538−4543.

(43) Herzberg, G. In *Molecular Spectra and Molecular Structure*; D. Van Nostrand Company, 1945.

(44) Fukui, K. Formulation of the reaction coordinate. *J. Phys. Chem.* **1970**, *74* (23), 4161−4163.

(45) Maranzana, A.; Ghigo, G.; Tonachini, G. Diradical and peroxirane pathways in the $[\pi2 + \pi2]$ cycloaddition reactions of $^1\Delta_g$ dioxygen with ethene, methyl vinyl ether, and butadiene: A density functional and multireference perturbation theory study. *J. Am. Chem. Soc.* **2000**, *122* (7), 1414−1423.

(46) Saito, T.; Nishihara, S.; Kataoka, Y.; Nakanishi, Y.; Kitagawa, Y.; Kawakami, T.; Yamanaka, S.; Okumura, M.; Yamaguchi, K. Reinvestigation of the reaction of ethylene and singlet oxygen by the approximate spin projection method. Comparison with multireference coupled-cluster calculations. *J. Phys. Chem. A* **2010**, *114* (30), 7967−7974.

(47) Saito, T.; Nishihara, S.; Kataoka, Y.; Nakanishi, Y.; Matsui, T.; Kitagawa, Y.; Kawakami, T.; Okumura, M.; Yamaguchi, K. Transition state optimization based on approximate spin-projection (AP) method. *Chem. Phys. Lett.* **2009**, *483* (1), 168−171.

(48) Lee, T. J.; Taylor, P. R. A diagnostic for determining the quality of single-reference electron correlation methods. *Int. J. Quantum Chem.* **1989**, *36* (S23), 199−207.

(49) Jayatilaka, D.; Lee, T. J. Open-shell coupled-cluster theory. *J. Chem. Phys.* **1993**, *98* (12), 9734−9747.

(50) Liakos, D. G.; Sparta, M.; Kesharwani, M. K.; Martin, J. M. L.; Neese, F. Exploring the accuracy limits of local pair natural orbital coupled-cluster theory. *J. Chem. Theory Comput.* **2015**, *11* (4), 1525−1539.

(51) Xu, X.; Muller, R. P.; Goddard, W. A. The gas phase reaction of singlet dioxygen with water: A water-catalyzed mechanism. *P. Natl. Acad. Sci. USA* **2002**, *99* (6), 3376−3381.

(52) Plesničar, B. Progress in the chemistry of dihydrogen dioxide (HOOOH). *Acta Chim. Slov.* **2005**, *52* (1), 1−12.

(53) Xiao, R.; Meng, Y.; Fu, Y.; Wacławek, S.; Wei, Z.; Spinney, R.; Dionysiou, D. D.; Zeng, W.; Hu, W. P. The overlooked carbonate radical in micropollutant degradation: An insight into hydration interaction. *Chem. Eng. J.* **2023**, *474*, 145245.

(54) Min, X.; Chu, C.; Luo, Z.; Ma, J.; Fu, Y.; Wei, Z.; Spinney, R.; Dionysiou, D. D.; Xiao, R. Transformation of phenol and nitrobenzene by superoxide radicals: Kinetics and mechanisms. *Chem. Eng. J.* **2022**, *442*, 136134.

(55) Connick, R. E. The Interaction of Hydrogen Peroxide and Hypochlorous Acid in Acidic Solutions Containing Chloride Ion. *J. Am. Chem. Soc.* **1947**, *69* (6), 1509−1514.

(56) Weil, I.; Morris, J. C. Kinetic studies on the chloramines. I. The rates of formation of monochloramine, N-chlormethylamine and N-chlordimethylamine. *J. Am. Chem. Soc.* **1949**, *71* (5), 1664−1671.

(57) Boudenne, J.-L.; Robert-Peillard, F.; Coulomb, B. Inorganic chloramines analysis in water. *Compr. Anal. Chem.* **2021**, *92*, 31−49.

(58) Lahoutifard, N.; Lagrange, P.; Lagrange, J. Kinetics and mechanism of nitrite oxidation by hypochlorous acid in the aqueous phase. *Chemosphere* **2003**, *50* (10), 1349−1357.

(59) Yang, Y.; Xiao, C.; Lu, J.; Zhang, Y. Fe(III)/Fe(II) forwarding a new anammox-like process to remove high-concentration ammonium using nitrate as terminal electron acceptor. *Water Res.* **2020**, *172*, 115528.

(60) Manickam, S.; Zainal Abidin, N. b.; Parthasarathy, S.; Alzorqi, I.; Ng, E. H.; Tiong, T. J.; Gomes, R. L.; Ali, A. Role of H_2O_2 in the fluctuating patterns of COD (chemical oxygen demand) during the treatment of palm oil mill effluent (POME) using pilot scale triple frequency ultrasound cavitation reactor. *Ultrason. Sonochem.* **2014**, *21* (4), 1519−1526.

(61) Guzman, J.; Mosteo, R.; Ormad, M. P.; Ovelleiro, J. L. Combined photo-fenton−SBR processes for the treatment of wastewater from the citrus processing industry. *J. Agric. Food Chem.* **2015**, *63* (2), 391−397.

(62) Barker, D. J.; Stuckey, D. C. A review of soluble microbial products (SMP) in wastewater treatment systems. *Water Res.* **1999**, *33* (14), 3063−3082.

(63) Fu, Y.; Yan, Y.; Wei, Z.; Spinney, R.; Dionysiou, D. D.; Vione, D.; Liu, M.; Xiao, R. Overlooked transformation of nitrated polycyclic aromatic hydrocarbons in natural waters: Role of self-photosensitization. *Environ. Sci. Technol.* **2023**, *57* (26), 9832−9842.

(64) Yan, Y.; Wei, Z.; Duan, X.; Long, M.; Spinney, R.; Dionysiou, D. D.; Xiao, R.; Alvarez, P. J. J. Merits and limitations of radical vs. nonradical pathways in persulfate-based advanced oxidation processes. *Environ. Sci. Technol.* **2023**, *57* (33), 12153−12179.

(65) Di Mascio, P.; Martinez, G. R.; Miyamoto, S.; Ronsein, G. E.; Medeiros, M. H. G.; Cadet, J. Singlet molecular oxygen reactions with nucleic acids, lipids, and proteins. *Chem. Rev.* **2019**, *119* (3), 2043−2086.